Natural Resources for Human Health
eISSN: 2583-1194

Original Research

Received 10 May 2026
Revised 15 June 2026
Accepted 02 July 2026

Natural Resources for Human Health 2026, Vol. 6 (4s): 238–251

KEYWORDS:
Ferrofluid; Shear thinning; Cross model; Carreau model; Viscoelasticty.

Cation Engineering in Spinel $M_{0.4}Fe_{2.6}O_4$ (M = Co, Mn, Zn) Ferrofluids: Correlating Crystal Structure, Magnetic properties, and Rheological Response

Arjun Singh[1,2,3*], Prashant Kumar[1,2,4], Preasha Rajput[5], Saurabh Pathak[6], R.P.Pant[1*]

[1]CSIR-National Physical Laboratory, Dr. K.S. Krishnan Marg, New Delhi-110012, India
[2]Academy of Scientific and Innovative Research (AcSIR), Ghaziabad, 201002, India
[3]Department of Physics, Indian Institute of Technology, Jammu, J&K-181221, India
[4]Next -Generation Magnet Development Collaboration Unit, RIKEN Center for Integrative Medical Sciences, Yokohama 230-0045, Japan
[5]Shri Mata Vaishno Devi University Katra, J&K-182320
[6]Center for Materials Innovation and Technology, Vin University, Hanoi, 100000, Vietnam
*Corresponding Authors: arjunsmy6@gmailcom, rppant@nplindia.org

ABSTRACT: Cation substitution provides an effective route for tailoring the magnetic and rheological properties of spinel ferrite ferrofluids. In this work, $Zn_{0.4}Fe_{2.6}O_4$ (ZFO), $Mn_{0.4}Fe_{2.6}O_4$ (MFO), and $Co_{0.4}Fe_{2.6}O_4$ (CFO) nanoparticles were synthesized under identical conditions and dispersed in kerosene to investigate the influence of divalent-cation chemistry on their structural, magnetic, and flow behaviour. X-ray diffraction confirmed the formation of the spinel ferrite structure, while FTIR and EDX analyses supported the formation of the respective metal–oxygen framework and elemental composition. Magnetic measurements revealed distinct saturation magnetization, coercivity, and effective anisotropy among the ferrofluids, demonstrating the influence of cation substitution on their magnetic characteristics. Rheological measurements under an applied magnetic field of 0.18 T over a shear-rate range of 1–1000 s^{-1} revealed pronounced shear-thinning behaviour for all three ferrofluids. The experimental viscosity data were satisfactorily described by the Power-law, Cross, and Carreau models. CFO exhibited the highest zero-shear viscosity and longest characteristic relaxation time, indicating comparatively stronger structural stability under low-shear conditions, whereas MFO showed the weakest rheological response. The results establish a clear relationship between cation chemistry, magnetic properties, field-induced nanoparticle organization, and shear-dependent flow behaviour, providing a pathway for tailoring spinel-ferrite ferrofluids for magnetically controlled applications.

Highlights

- Zn-, Mn-, and Co-substituted spinel ferrite ferrofluids were successfully synthesized and systematically compared.
- Cation substitution strongly modulates the structural and magnetic properties of the ferrofluids.

- All ferrofluids exhibit pronounced shear-thinning behaviour under an applied magnetic field of 0.18 T.
- Power-law, Cross, and Carreau models successfully describe the shear-dependent viscosity and structural relaxation.
- CFO exhibits the strongest low-shear structural stability, highlighting cation chemistry as an effective route for tailoring ferrofluid rheology.

1. INTRODUCTION

Ferrofluids are unique nanofluids in which microscopic magnetic interactions at the nanoscale can finely tune macroscopic fluid properties, such as viscosity and flow behaviour, under an external magnetic field[1–5]. The combination of magnetism and fluidity, together with their ability to dynamically assemble, reorganize, and restructure magnetic nanoparticle networks in response to an applied magnetic field, makes ferrofluids promising functional materials for emerging applications in microfluidics, soft robotics, lubrication, heat transfer, damping, and actuation, as well as biomedical applications such as targeted drug delivery, magnetic resonance imaging (MRI), biosensing, and magnetic hyperthermia. However, conventional ferrofluids often face challenges associated with limited colloidal stability, nanoparticle agglomeration, and inadequate magnetic-field responsiveness. These limitations can be addressed through careful control of nanoparticle size and size distribution, surface coating, particle stoichiometry, and compatibility between the magnetic nanoparticles and the carrier medium[6–12].

Ferrofluids can be formulated using various types of magnetic nanoparticles; however, spinel ferrites (MFe_2O_4) provide a versatile platform for tailoring magnetic interactions through controlled cation chemistry and distribution. The spinel lattice consists of tetrahedral (A) and octahedral (B) cation sites, whose occupancy by divalent and trivalent cations can be modified depending on the nature of the substituting ion, synthesis conditions, and degree of cation inversion. Such variations in cation distribution strongly influence the magnetic exchange interactions, magnetization, magnetocrystalline anisotropy, and coercivity of the ferrite nanoparticles. In particular, Zn^{2+}, Mn^{2+}, and Co^{2+} ions impart distinctly different magnetic characteristics to the spinel lattice. Co^{2+}-containing ferrites generally exhibit high magnetocrystalline anisotropy and enhanced coercivity, whereas Mn^{2+}-containing ferrites are typically characterized by relatively low coercivity and soft-magnetic behaviour. Zn^{2+}, being a non-magnetic cation, can significantly modify the cation distribution and magnetic exchange interactions; at moderate Zn substitution levels, it can enhance the saturation magnetization by altering the balance between the A- and B-site magnetic sublattices, whereas excessive Zn substitution can weaken the A–B superexchange interaction and lead to a pronounced reduction in magnetization, eventually approaching paramagnetic behaviour at sufficiently high Zn concentrations[13–17]. The macroscopic flow behaviour of the synthesized ferrofluids strongly depends on the intrinsic microscopic magnetic properties of the nanoscale magnetic particles dispersed in the carrier liquid. The magnetic dipoles tend to align with the external magnetic field, resulting in the formation of chain-like and cluster-like structures through magnetic dipole–dipole interactions. The stability and structure of these field-induced chain networks depend on various properties of the dispersed magnetic nanoparticles, such as magnetocrystalline anisotropy, saturation magnetization, particle size, and interparticle interactions. These parameters can be effectively modified by maintaining the stoichiometry of the substituted cations within the overall spinel ferrite framework. Therefore, ferrofluids based on $Zn_{0.4}Fe_{2.6}O_4$ (ZFO), $Mn_{0.4}Fe_{2.6}O_4$ (MFO), and $Co_{0.4}Fe_{2.6}O_4$ (CFO), synthesized at an identical substitution concentration under comparable conditions, provide a useful model system for systematically understanding the role of cation chemistry in regulating magnetic-field-induced structural organization and flow behaviour. When an external shear is applied, the hydrodynamic forces act against the magnetic dipolar interactions, leading to the deformation, disruption, and reorganization of the transient nanoparticle networks. Consequently, the shear-dependent viscosity, degree of shear thinning, and structural disruption are determined by the relative strength of the hydrodynamic and magnetic interactions[18].

Extensive literature is available on the structural and magnetic properties of spinel-ferrite-based magnetic nanoparticles; however, a clear relationship linking cation chemistry, magnetic characteristics, and the rheological response of their ferrofluids has not yet been established[14,19,28–31,20–27]. In particular, a systematic comparison of ferrofluids containing different divalent cations at an identical substitution concentration can provide deeper insight into how tailored magnetic properties influence the magnetic nanoparticle chain networks and flow behaviour under an applied magnetic field. Thus, the incorporation of $Zn_{0.4}Fe_{2.6}O_4$, $Mn_{0.4}Fe_{2.6}O_4$, and $Co_{0.4}Fe_{2.6}O_4$ provides a suitable model system in which the effect of cation chemistry can be explored while maintaining the same substitution concentration. This controlled composition enables us to distinguish the individual contributions of magnetic parameters, such as magnetocrystalline anisotropy, saturation magnetization, and microscopic interparticle interactions, to the field-induced viscosity and shear-dependent response. Furthermore, the formation,

restructuring, and relaxation behaviour of the magnetic nanoparticle networks under shear can be quantitatively analysed using suitable rheological models[13,18,32–36].

In the present work, spinel ferrite nanoparticles with the nominal composition $M_{0.4}Fe_{2.6}O_4$ (M = Co, Mn, and Zn) were synthesized via a controlled co-precipitation route and subsequently dispersed in a kerosene medium to formulate stable ferrofluids. The influence of cation substitution on the crystal structure, microstructure, elemental composition, magnetic properties, and rheological response was systematically investigated using X-ray diffraction (XRD), Fourier-transform infrared (FTIR) spectroscopy, energy-dispersive X-ray spectroscopy (EDX), vibrating sample magnetometry (VSM), and steady-shear rheological measurements under a constant magnetic field of 0.18 T. Particular emphasis was placed on establishing correlations between cation chemistry, magnetic properties, interparticle interactions, and flow behaviour. The experimental rheological data were further analysed using Power-law, Cross, and Carreau models to quantify the shear-thinning behaviour, limiting viscosities, and characteristic relaxation of the ferrofluids. The findings provide insights into the role of cation substitution in modulating the coupled magnetic and rheological properties of spinel-ferrite-based ferrofluids and provide a basis for tailoring their flow response for potential technological and biomedical application.

2. EXPERIMENTAL DETAILS

2.1 Synthesis

The non stoichiometric Iron rich $M_xFe_{3-x}O_4$ (x = 0.4) MNPs (with M = Co, Mn, Zn)(MFO) are synthesised by facile varying chemical co-precipitation method. The high purity (> 99.9%, Sigma Aldrich) $FeCl_3$, $CoCl_2$, $MnCl_2$ and $ZnCl_2$ salts are taken into stoichiometric amounts for making solution in DI water independently and thereafter mixed under constant stirring for 45 minutes at 80°C. To this solution, 5M NH_4OH is added dropwise until it reached a pH value of 10. The precipitated mixture was maintained at constant temperature of 80°C for 60 minutes under constant stirring to propel homogeneous nucleation and growth. The black precipitates were washed several times with distilled water and organic solvents using magnetic decantation. The particles are dried in a vacuum oven and are used for further characterization.

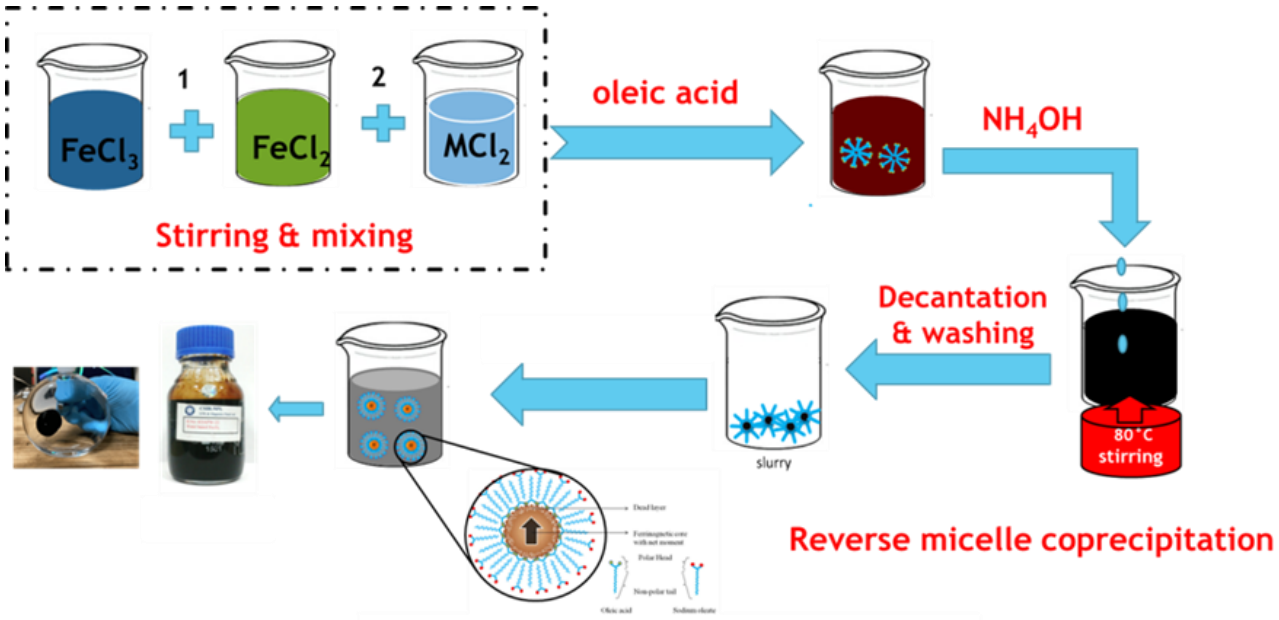

Figure 1 : Schematic illustration of the synthesis procedure for $Zn_{0.4}Fe_{2.6}O_4$ (ZFO), $Co_{0.4}Fe_{2.6}O_4$ (CFO), and $Mn_{0.4}Fe_{2.6}O_4$ (MFO) magnetic nanoparticles, followed by the preparation of highly stable kerosene-based ferrofluids through oleic acid surface modification. Here, **M** denotes Zn, Co, or Mn.

2.2 Characterization

The phase formation and crystalline quality of synthesized magnetic nanoparticles based ferrofluid are examined with multipurpose X-ray diffractometer (MXRD, Rigaku ultima-IV) and the patterns are analyzed with structural retvield refinement

in the theta range from 20° to 70° with resolution of 0.02° using FullProf Software. The elemental composition and stoichiometry is confirmed with EDAX (Rigaku ZSX primus) technique (presented in supplementary section). The particle size distribution is studied with high resolution transmission electron microscope (HRTEM, TECNAI F30 model) and particle histogram is calculated through lognormal distribution function. The Fourier transform infrared (FTIR) spectra are recorded with NICOLET 5700 in the range 2500-400 cm^{-1} (presented in supplementary section). The room temperature static magnetization is recorded with Vibrating sample magnetometer (VSM, Lakeshore 7304). Rheological measurements were conducted using the Anton Paar GmbH MCR 301 parallel plate magneto-rheometer, equipped with the standard MRD-70 rotation geometry and a PP-20 spindle. A transverse magnetic field of 0.18T was applied between the plates while a thermostatic bath was used to maintain a room temperature and measurements were performed from varying shear rate from $1s^{-1}$ to $1000s^{-1}$. The gap between the parallel plates was set at 1 mm. Before the experiment, samples were pre-sheared at 20 s-1 for 30 s.

3. RESULTS AND DISCUSSION

3.1 Structural Analysis

The room temperature Powder X-ray diffraction patterns for $Zn_{0.4}Fe_{2.6}O_4$ (ZFO), $Co_{0.4}Fe_{2.6}O_4$ (CFO), and $Mn_{0.4}Fe_{2.6}O_4$ (MFO) are shown in **Figure 2 (a)**. The observed diffraction peaks, show well-defined reflections corresponding to the crystallographic planes (220), (311), (400), (422), (511) and (440) which are indexed to face-centered cubic structure with the $Fd\bar{3}m$ space group. Among these planes, the highest intensity (311) planes confirm the successful formation of spinel single phase with no additional impurity in the synthesis. A relative peak shift is observed with cation substitution, due to differences in cationic size and site-occupancy preferences among Zn2+, Co2+, and Mn^{2+} ions. The measured cubic unit cell dimensions are 8.39±0.02 Å for ZFO, 8.38±0.02 Å for CFO and 8.37±0.02 Å for MFO. The slightly larger dimensions of ZFO can be attributed to the larger ionic radii of tetrahedrally preferred Zn^{2+} ions. To obtain quantitative structural information, the diffraction data were refined using the Rietveld method, and the refinement profiles are presented in **Figures 2(b–d).** The excellent agreement between the observed diffraction intensities, calculated profiles, Bragg reflection positions, and difference curves demonstrates the high quality of the structural refinement. The refinement converged with low profile agreement factors of Rp = 2.94–3.09%, Rwp = 3.65–3.85%, and goodness-of-fit values (χ^2 = 2.43–2.61), confirming the reliability of the refined structural model. Furthermore, the refined oxygen positional parameter (u = 0.252-0.259) remains close to the ideal value expected for cubic spinel ferrites, suggesting only a slight distortion of the oxygen framework. The marginally higher oxygen parameter observed for CFO indicates a small modification of the metal–oxygen bond geometry resulting from the stronger crystal-field stabilization and spin–orbit coupling associated with Co^{2+} ions.

The refined cation distribution further reveals the influence of cation substitution on the spinel structure. In the ZFO sample, Zn^{2+} ions preferentially occupy the tetrahedral (A) sites along with Fe^{3+} ion, while Fe^{2+} and Fe^{3+} ions mainly reside at the octahedral (B) sites, corresponding to a partially inverse spinel configuration, On the other hand, Co^{2+} ions exhibit a strong preference for the octahedral sites in CFO, whereas the tetrahedral sites remain predominantly occupied by Fe^{3+} ions, consistent with the characteristic inverse spinel structure of cobalt ferrite. For MFO, Mn^{2+} ions are distributed between both tetrahedral and octahedral sites, resulting in a partially inverse spinel arrangement[37].

The crystal structures visualized with VESTA software are shown in Figure 3, which provides a three-dimensional representation of the cubic spinel unit cell. The spinel crystal structure is based on a face-centered cubic (FCC) arrangement of oxygen anions (O^{2-}), containing eight formula units per unit cell (Z = 8). The cubic close-packed oxygen lattice creates two types of interstitial sites: 64 tetrahedral (A) sites and 32 octahedral (B) sites per unit cell. Of these, only 8 tetrahedral and 16 octahedral sites are occupied by cations, while the remaining interstitial sites remain vacant. The distribution of cations between the A and B sites depends on their ionic size, valence state, crystal-field stabilization energy, and synthesis conditions. In normal spinels, Zn^{2+} preferentially occupies the tetrahedral (A) sites, whereas Co^{2+} preferentially occupies the octahedral (B) sites. Mn^{2+} can occupy both tetrahedral and octahedral sites, leading to a mixed cation distribution depending on the degree of inversion and preparation conditions.

The crystallite size and lattice strain were further estimated using the Williamson–Hall (W–H) method, and the corresponding plots are presented in **Figure 2(e)**. The average crystallite sizes were found to be **12 ± 2 nm** for ZFO, **10 ± 2 nm** for MFO, and **9 ± 2 nm** for CFO, whereas the corresponding lattice strains remain low (**0.004–0.005**), indicating good crystallinity with minimal microstructural distortion. The particle sizes determined from TEM (**10–16 nm**) as shown in **Figure 4** are slightly

larger than the crystallite sizes obtained from XRD, suggesting that individual nanoparticles consist of one or a few coherently diffracting crystallites. The slight reduction in crystallite size following Co and Mn substitution indicates that these cations suppress crystal growth during nucleation, resulting in finer nanoparticles.

The fine structural modifications induced by Zn^{2+}, Co^{2+}, and Mn^{2+} substitution are expected to alter the A–O–B super exchange interactions and is expected to tune the effective magnetic anisotropy, dipolar interaction, and hence found prevailing for understanding the magnetic and rheological behavior of the corresponding ferrofluids discussed in the subsequent sections.

Table 1(a) : Structural parameters of $Zn_{0.4}Fe_{2.6}O_4$ (ZFO), $Co_{0.4}Fe_{2.6}O_4$ (CFO), and $Mn_{0.4}Fe_{2.6}O_4$ (MFO) magnetic nanoparticles

Sample	Crystallite size (D) (WH method) (nm)	Particle size (TEM) (nm)	Lattice parameter (Å)	Lattice strain (ϵ)	X-ray density g/cm^3	Volume (Å^3)
ZFO	12±2	16±2	8.39±0.02	0.005(1)	5.29	590±3
MFO	10±2	12±2	8.37±0.02	0.004(1)	5.23	586±3
CFO	9±2	10±2	8.38±0.02	0.004(1)	5.29	588±3

Table 1(b) : Rietveld refinement parameters of $Zn_{0.4}Fe_{2.6}O_4$ (ZFO), $Co_{0.4}Fe_{2.6}O_4$ (CFO), and $Mn_{0.4}Fe_{2.6}O_4$ (MFO) magnetic nanoparticles

Sample	R-factors			χ^2	Oxygen position (u)	Tetrahedral (A-site) (x=y=z=0.125)	Octahedral (B-site) (x=y=z=0.5)
	R_p (%)	R_{wp} (%)	R_{exp} (%)				
ZFO	2.97	3.73	2.39	2.43	0.252	$Zn^{2+}_{0.39}Fe^{3+}_{0.61}$	$Fe^{2+}_{0.6}Fe^{3+}_{1.4}$
MFO	3.09	3.85	2.41	2.57	0.254	$Mn^{2+}_{0.1}Fe^{3+}_{0.9}$	$Mn^{2+}_{0.3}Fe^{2+}_{0.6}Fe^{3+}_{1.1}$
CFO	2.94	3.65	2.26	2.61	0.259	$Fe^{3+}_{1.0}$	$Co^{2+}_{0.4}Fe^{2+}_{0.6}Fe^{3+}_{1.0}$

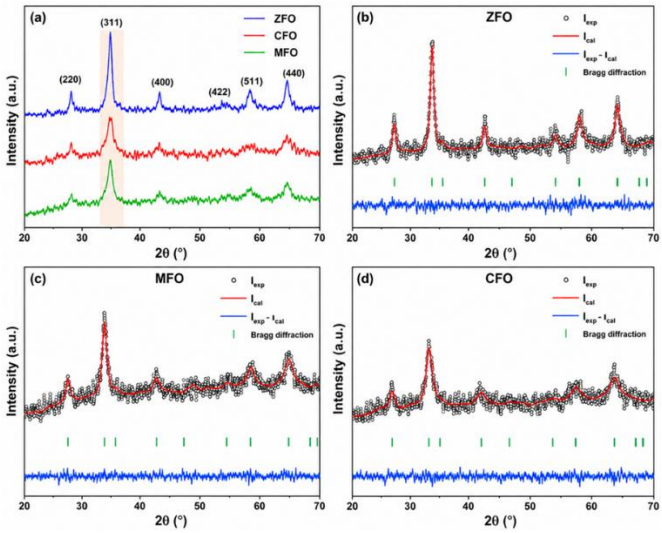

Figure 2 : (a) Powder X-ray diffraction (PXRD) patterns of $Zn_{0.4}Fe_{2.6}O_4$ (ZFO, blue), $Co_{0.4}Fe_{2.6}O_4$ (CFO, red), and $Mn_{0.4}Fe_{2.6}O_4$ (MFO, green) magnetic nanoparticles. The diffraction peaks confirm the formation of a single-phase spinel crystal structure without any detectable impurity phases. (b) Rietveld refinement of the PXRD pattern for ZFO. (c) Rietveld refinement of the PXRD pattern for MFO. (d) Rietveld refinement of the PXRD pattern for CFO.

Natural Resources for Human Health
eISSN: 2583-1194

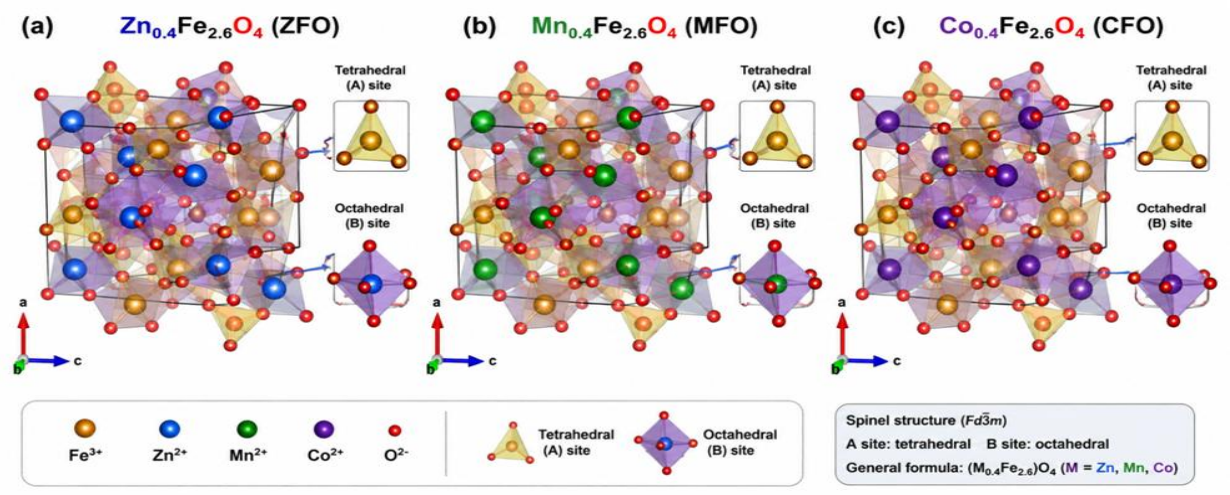

Figure 3 : Crystal structures generated using VESTA after importing the Crystallographic Information File (CIF) obtained from Rietveld refinement with the lowest χ^2 value. (a) Spinel crystal structure of $Zn_{0.4}Fe_{2.6}O_4$ (ZFO), where Zn^{2+} preferentially occupies the tetrahedral (A) sites, exhibiting a mixed spinel structure. (b) Spinel crystal structure of $Mn_{0.4}Fe_{2.6}O_4$ (MFO), where Mn^{2+} preferentially occupies both (10%) tetrahedral (A) and (90%) octahedral (B) sites, resulting in mixed spinel structure. (c) Spinel crystal structure of $Co_{0.4}Fe_{2.6}O_4$ (CFO), where Co^{2+} preferentially occupies the octahedral (B) sites, forming an inverse spinel structure.

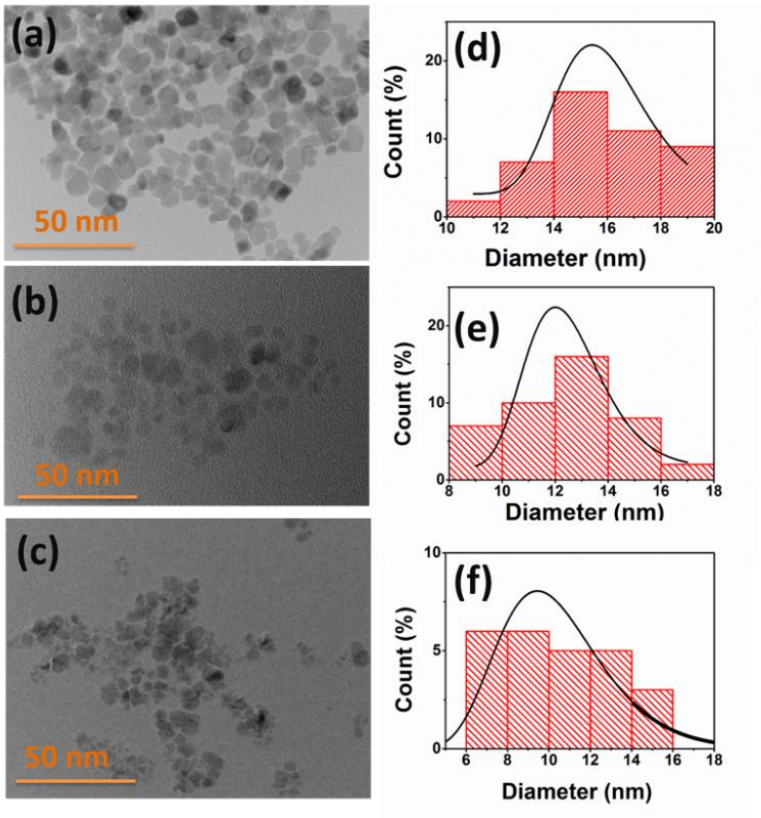

Figure 4 : TEM micrographs of (a) $Zn_{0.4}Fe_{2.6}O_4$ (ZFO), (b) $Mn_{0.4}Fe_{2.6}O_4$ (MFO), and (c) $Co_{0.4}Fe_{2.6}O_4$ (CFO) magnetic nanoparticles. The corresponding particle size distribution histograms derived from the TEM images are presented in (d) ZFO, (e) MFO, and (f) CFO.

3.2 Static magnetization Analysis

The magnetic characteristics of the synthesized ferrite nanoparticles were investigated using vibrating sample magnetometry (VSM) at room temperature under an applied magnetic field ranging from -20 kOe to +20 kOe. The obtained MH loops for each sample are shown in Figure 5, which depict a ferrimagnetic nature with relatively low coercivity, indicating a soft magnetic nature. Among all the samples, $Zn_{0.4}Fe_{2.6}O_4$ (ZFO) shows the highest saturation magnetization of 59.4 emu/g. This enhancement may be attributed to the preferential occupation of nonmagnetic Zn^{2+} ions at tetrahedral (A) sites, which forces Fe^{3+} ions to migrates towards octahedral (B) sites. Thus, the net magnetic moment between the A and B sublattices increases, leading to higher magnetization according to Néel's two-sublattice model, as shown in **Figure 5(b)**. The $Co_{0.4}Fe_{2.6}O_4$ (CFO) sample exhibits the highest coercivity value of 94 G among all investigated samples. This behavior is usually associated with the single-ion anisotropy of Co^{2+} ions, resulting in enhanced spin–orbit interaction. The increased anisotropy provides resistance to the movement of the domain, which results in an increase in coercivity. The results show lower saturation magnetization for $Mn_{0.4}Fe_{2.6}O_4$ (MFO), which may be related to spin canting effects and weaker superexchange interactions between tetrahedral and octahedral sites, as discussed in the structural section. Surface disorder and non-collinear spin arrangements in nanoscale particles can further reduce the net magnetic moment. The low coercivity values observed for ZFO and MFO indicate soft-magnetic behavior, which is desirable for applications in transformer cores, magnetic fluids, and high-frequency magnetic devices. The experimentally observed magnetic moments are 1.9 μB, 1.5 μB, and 1.2 μB for ZFO, CFO, and MFO, respectively, as shown in Table 2, and follow the same trends as saturation and confirm the cation redistribution effect. The effective anisotropy constant (K_{eff}) was estimated using the magnetic parameter obtained from the hysteresis loop using the relation ($H_c = 2K_{eff}/\mu_0 m_s$). Among all investigated samples, CFO exhibits the highest anisotropy constant, primarily attributed to the strong spin-orbit coupling. The comparatively lower anisotropy constant observed for MFO may be associated with increased surface spin disorder and spin-canting effects at the nanoscale. The squareness ratio (M_r/M_s) was found to be 0.049, 0.085, and 0.048 for ZFO, CFO, and MFO, respectively. The low squareness ratios indicate soft-magnetic behavior and higher surface spin disorder and thermal fluctuations. The highest observed squareness of CFO, is consistent with its enhanced coercivity and effective anisotropy arising from the strong spin–orbit coupling of Co^{2+} ions. The experimental observed values are considerably lower than the theoretical Stoner–Wohlfarth limit of 0.5, indicating non-ideal magnetic ordering and possible spin canting effects in the nanoparticles[38]. The experimental magnetic moments are observed at lower values compared to the theoretical ones, which can be attributed to two reasons: one, a change in the spin structure from collinear to non-collinear, and two, the surface spin-canting effect, which predominates at the nanoscale. These results demonstrate that magnetic properties can be effectively tailored through selective cation substitution, making the synthesized ferrites promising candidates for soft magnetic, ferrofluid, and high-frequency magnetic applications.

Table 2: Magnetic parameters obtained from VSM measurement

Sample	Coercivity (H_c) (Oe)	m_s (emu/g)	Magnetic moment (μ_B)	Effective anisotropy(K_{eff}) (Kerg/cm^3)	Squareness ratio (mr/ms	Yafet kittel angle (°)
ZFO	26±2	59±2	1.9	4.2±0.2	0.05(2)	59(1)
MFO	23±2	40±2	1.5	2.5±0.2	0.05(2)	49(1)
CFO	94±3	46±2	1.2	11.9±0.3	0.009(2)	41(1)

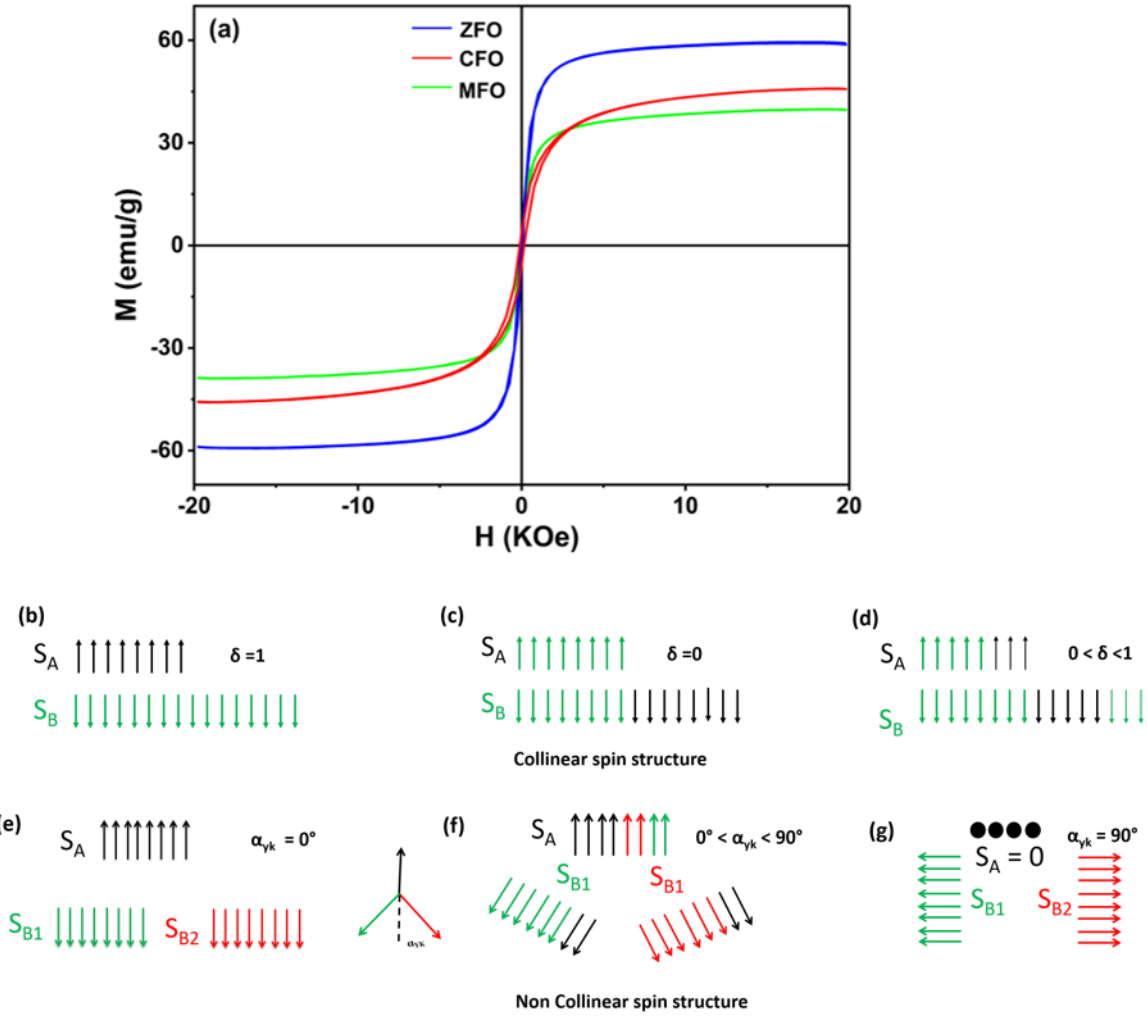

Figure 5 (a) Magnetization (*M*) versus applied magnetic field (*H*) curves of $Zn_{0.4}Fe_{2.6}O_4$ (ZFO), $Mn_{0.4}Fe_{2.6}O_4$ (MFO), and $Co_{0.4}Fe_{2.6}O_4$ (CFO) magnetic nanoparticles measured at room temperature. (b–g) Schematic illustrations of the evolution of collinear and non-collinear spin configurations induced by cation substitution, highlighting the redistribution of cations between tetrahedral (A) and octahedral (B) sites, modification of A–B superexchange interactions, and the emergence of Yafet–Kittel-type spin canting.

3.3 Rheology of Ferrofluids

Rheological behaviour

The flow characteristics of the synthesized ZFO, MFO, and CFO ferrofluids was explored under a static magnetic field of 0.5 T (~2A) using parallel plate magnetorheometer. The steady state visocosity was measured over a significant shear rate variation of (1-1000 s^{-1}) to understand the effect of cation substitution on shear-induced microstructural transformation and flow behaviour at static field. Figure 6(a) represents the experimental observed rheogram data for all the three different compostions. The data were further analysed with well established theoretical models (Power-law, Cross model, and Carreau models) to obtain insight about low shear micorstructure, strctural breakdown at moderate shear rate and further relaxation behaviour of ferrofluid.

The Power-law model[8] was first employed to characterize the shear-dependent flow behaviour, which is expressed as

$$\eta = K\dot{\gamma}^{n-1}$$

where η is the apparent viscosity , (K) is the consistency coefficient, ($\dot{\gamma}$) is the shear rate, and (n) is the flow behaviour index.

The index behaviour n determines the fluid behaviour, for n = 1, represents Newtonian whereas n ≠ 1 represents as non-Newtonian with (n<1) indicates shear-thinning and (n>1) represents shear-thickening behaviour. **Figure 6(b)** shows that experimental data unviel excellent agreement with the Power-law description, with coefficients of determination in the range (R^2=0.95-0.99)[39]. The negative values of the exponent obtained from the viscosity representation confirm pronounced shear-thinning behaviour for all three ferrofluids. Thus, the apparent viscosity decreases continuously with increasing shear rate. The obtained pseudoplastic behaviour is primarily due to field induced alignment of magnetic nanoparticles as presented in **Figure 7**. It is observed that at very low shear rates, the apparent viscosity is large (>100mPa s) which is due to dominance of dipole-dipole interaction (formations of chain like aggregiagtes under applied external magnetic field) and brownian motion. As the shear rate increases beyond the crtical value, dipolar interactions and brownian effect start weakening and thus result there is misalignment or breaking of chain like structure. The hydrodynamic forces acting on the fluid particles now increases and start dominating with increasing shear rate Finally the magnetic particles aligned with the flow at very high shear rate (>100-200 s^{-1}) and the viscosity apparently to be very small (2-3mPa s). The rheological response therefore reflects the competition between magnetic interactions, Brownian motion, and hydrodynamic forces.

The CFO exhibits strong shear-dependent response whereas MFO observes weakest departure to Newtonian behaviour. The distinction is assciated with variation in the cationic substituion of the differently composed magnetic nanoparticle based ferrofluid. The CFO exhibist highest magnetocrystalline anisotropy of supports stronger dipolar interactions and provides smooth transient particle network. The CFO ferrofluid display high resistance at low shear rates and more significant microstrcutural breaks when applied shear rate is increased. Whereas, the MFO has comparatevly weaker magnetic coupling results in a less strongly interconnected transient structure and comparatively weaker shear-dependent viscosity reduction rate.

To understand further the complete description of the viscosity behaviour over the entire range of shear-rate, the experimental data is fitted using the Cross model [40]and is presented in **Figure 6(c)**.

$$\eta = \eta_\infty + \frac{\eta_0 - \eta_\infty}{1 + (k\dot{\gamma})^m}$$

where η_∞ is the infinite-shear viscosity, η_0 is the zero-shear viscosity, k is the characteristic time associated with shear induced particle network (chain arrangement), and m is the Cross-model shear-thinning index parameter. The fitted parameters are summarized in **Table 3** . The infinite-shear viscosity remains within a narrow range of 1.31-1.53 mPa s with values of 1.33, 1.31, and 1.53 mPa·s for ZFO, MFO, and CFO, respectively. The small variation in infinite shear viscosity (η_∞) indicates that at sufficiently high shear rate, the viscosity is predominatly due to hydrodynamics interaction and carrier medium (kersone) and field induced nanoparticle network effect is negligilbe.

Further, the distiguishable compositional effect is observed in the zero-shear viscosity. The values follow the order η_0 (CFO) > η_0 (ZFO) > η_0 (MFO), with 488, 446 and 201mPa s respectively. The ~ 2.4 time higher zero-shear viscosity of CFO is comparatevly MFO suggests that there is more stronger flow resistance at applied low shear rate for CFO. Further, we can conclude that CFO has strong field induced particle network at low shear rate. Further, ZFO also shows a considerably higher η_0 than MFO, suggesting stronger interparticle interaction and MFO reveals to be the weakest strctural repsonse among the three candidates. This can be further understand by the characteristics time parameter (k) which measure the transtion time from low shear viscosity (η_0) towards high shear viscosity (η_∞). The larger value of k signifies the structural breakdown start occurs at low shear rate whereas smaller value of k tells that structural transformation happens at large shear rate. Among investigated compostions, the CFO posseses larger k value which suggests that its microstructural transformation happens faster due to large and comparatevly stronger particle network. On the other side, the small value obtained for MFO indicates that its microstructure response is slower due to weak particle network on small induced shear rate. The Cross-model exponent (m) observed to 0.86, 0.96, and 0.91 for ZFO, MFO, and CFO, respectively with coefficient of determination R^2 is 0.99. The fitted parameters confirm that the viscosity reduction with shear is composition dependent and is associated with progressive disruption of the field-induced nanoparticle structure.

The rheological obervations were further anlysed through Carreau model[41] as shown in **Figure 6 (d)**

$$\eta = \eta_\infty + (\eta_0 - \eta_\infty)[1 + (\lambda\dot{\gamma})^2]^{\frac{(n-1)}{2}}$$

Where λ is the characteristic relaxation time and n is the Carreau flow behaviour index. The λ obtained from Carreau analysis gives 0.75s, 0.17s, and 0.84s for ZFO, MFO, and CFO, respectively. The larger relaxation value of CFO is attributed to strong magnetic coupling and large magnetocrystalline anisotropy which results require more time to realign the particle network shear force is removed. In contrast MFO observed to smallest relaxation value which suggests its soft magnetic nature and thus results faster structural rearrangement and produces weakly interconnected nanoparticle network. The sample ZFO is showing an intermediate relaxation among them.

The Carreau flow index (n) values are 0.48, 0.52, and 0.46 for ZFO, MFO, and CFO, respectively confirming further sheartheaning non-Newtonian behaviour with n < 1. The obtained bahviour is consistent with power law for all three systems. The lower (n) value for CFO (n=0.46) exhibits the strongest shear-thinning response according to the Carreau model, closely followed by ZFO (n=0.48), whereas MFO (n=0.52) display the weakest shear-thinning behaviour. The difference in the index paramters between Power-law and Carreau fits is because of the difference in the fitiing pattern of the experiemntal data. Generally, the power laws the primarily means for power law region (generally good for small shear rate), whereas the Carreau model pictures transitional phase between the low and high viscosity shear ranges. These results establish that the magnetic properties of the ferrite phase, particularly the magnetic anisotropy and associated dipolar interactions, play a crucial role in determining the macroscopic flow behaviour and structural dynamics of the ferrofluids. Therefore, controlled cation substitution provides an effective strategy for tailoring the viscosity, shear response, and structural relaxation characteristics of spinel-ferrite-based ferrofluids for applications requiring externally controllable flow properties.

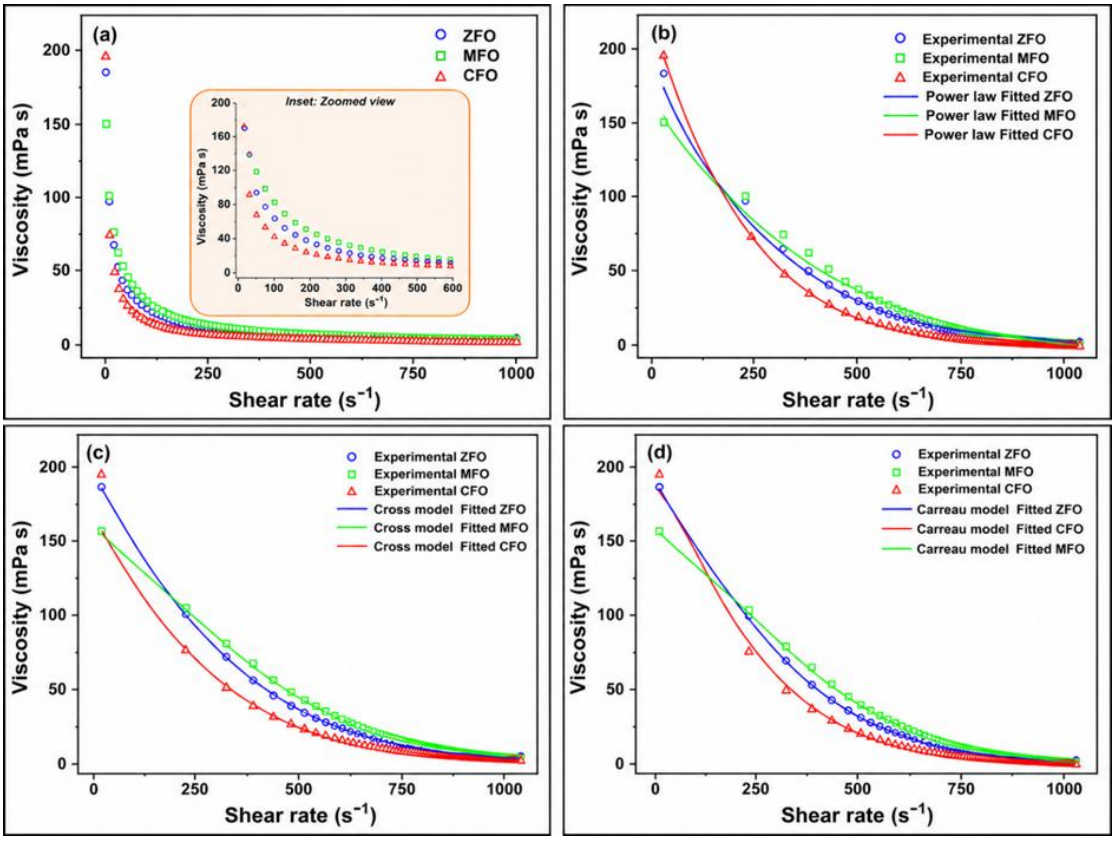

Figure 6 (a) Shear viscosity as a function of shear rate for ZFO, MFO, and CFO ferrofluids (linear scale X-axis with inset log scale with zoom view). Comparison of experimental data with fitted (log scale X-axis) curves using the (b) Power-law, (c) Cross, and (d) Carreau rheological models.

Natural Resources for Human Health
eISSN: 2583-1194

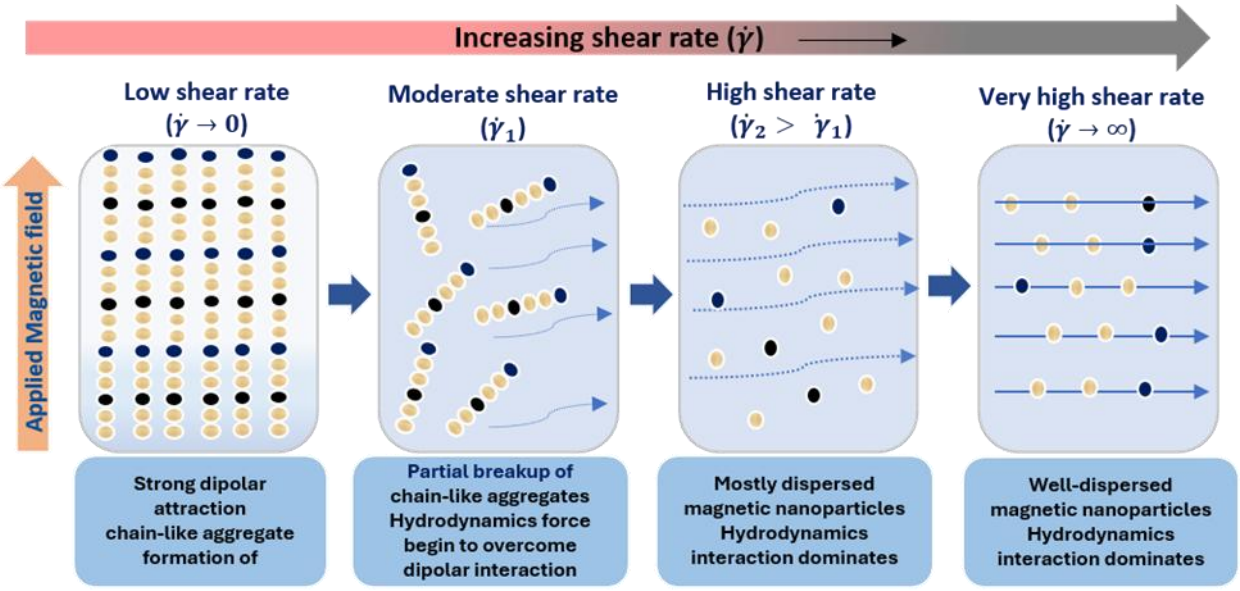

Figure 7 : Schematic illustration of the evolution of magnetic nanoparticle microstructure under an applied magnetic field with increasing shear rate, showing the transition from chain-like aggregates at low shear rates to well-dispersed nanoparticles at very high shear rates due to the dominance of hydrodynamic forces over dipolar interactions.

Table 3 : Fitted parameters obtained from steady state flow curve

Sample	Power law	Cross model fit paramters			Carreau model fit paramters		
	n-1	η_∞ (mPa s)	η_0 (mPa s)	k (s)	(m)	λ(s)	n
ZFO	-0.75	1.33	446 ± 10	1.44	0.86	0.75	0.48
MFO	-0.66	1.31	201± 8	0.33	0.96	0.17	0.52
CFO	-0.89	1.53	488± 10	2.00	0.91	0.84	0.46

CONCLUSION

In conclusion, $Zn_{0.4}Fe_{2.6}O_4$ (ZFO), $Mn_{0.4}Fe_{2.6}O_4$ (MFO), and $Co_{0.4}Fe_{2.6}O_4$ (CFO) spinel ferrite nanoparticles were successfully synthesized at an identical substitution concentration and formulated into stable kerosene-based ferrofluids. The structural and magnetic characterizations confirmed the formation of spinel ferrite phases, while the observed differences in saturation magnetization, coercivity, and magnetocrystalline anisotropy demonstrated the strong influence of the substituted divalent cation on the magnetic characteristics of the nanoparticles. Among the investigated compositions, ZFO exhibited the highest saturation magnetization, whereas CFO showed the highest coercivity and effective magnetic anisotropy, reflecting stronger magnetic interactions and a comparatively robust nanoparticle microstructure.

The rheological measurements performed under an applied magnetic field of 0.18 T revealed pronounced non-Newtonian and shear-thinning behaviour for all three ferrofluids. The viscosity decreased progressively with increasing shear rate as the hydrodynamic forces progressively disrupted and reorganized the field-induced nanoparticle networks. The experimental flow curves were successfully described by the Power-law, Cross, and Carreau models, with all models providing satisfactory agreement with the experimental data. The Power-law and Carreau flow indices remained below unity, independently demonstrating the pseudoplastic nature of the ferrofluids. The Cross and Carreau analyses further revealed significant differences in the zero-shear viscosity and characteristic relaxation times among the compositions, with CFO exhibiting the highest zero-shear viscosity and longest characteristic relaxation time, indicating greater low-shear structural stability.

The comparative rheological response demonstrates that cation substitution at a fixed concentration provides an effective means of tailoring the flow characteristics of spinel-ferrite-based ferrofluids. The observed differences arise from the interplay between magnetic anisotropy, saturation magnetization, dipole–dipole interactions, Brownian motion, and hydrodynamic forces, which collectively determine the formation and shear-induced restructuring of transient nanoparticle networks. Thus, controlling the identity of the divalent cation provides a practical route for tuning the magnetic and rheological response of ferrofluids, with potential relevance to magnetically controlled damping, actuation, heat-transfer, microfluidic, and biomedical applications.

ACKNOWLEDGEMENTS

The authors would like to thank the Director, CSIR–National Physical Laboratory (CSIR–NPL), New Delhi, for constant encouragement, support, and providing the necessary facilities for carrying out this research work. Dr. Arjun Singh gratefully acknowledges the Director, Indian Institute of Technology Jammu, for providing access to and support from the Central Instrumentation Facility (CIF) for the characterization and analysis carried out in this work.

AUTHOR CONTRIBUTIONS

Arjun Singh: Conceptualization, investigation, data analysis, and writing – original draft.

Prashant Kumar: Magnetic characterization and analysis.

Preasha Rajput: Rietveld refinement and analysis.

Saurabh Pathak: Review and editing.

R. P. Pant**:** Supervision, review and editing.

CONFLICT OF INTEREST

The authors declare that there is no conflict of interest.

ETHICS STATEMENT : Ethical approval was not required for this study.

DATA AVAILABILITY STATEMENT

Data supporting the findings of this study are available from the corresponding author upon reasonable request.

REFERENCES

[1] Singh A, Kumar P, Pathak S, et al. A threefold increase in SAR performance for magnetic hyperthermia by compositional tuning in zinc-substituted iron oxide superparamagnetic nanoparticles with superior biocompatibility. *J Alloys Compd*. 2023;968:171868. doi:https://doi.org/10.1016/j.jallcom.2023.171868

[2] Singh A, Kumar P, Rajput P, et al. Investigating the impact of zinc ion substitution on the rheological properties and hyperthermia potential of cobalt ferrite-based ferrofluids. *Mater Today Proc*. Published online 2023. doi:https://doi.org/10.1016/j.matpr.2023.05.479

[3] Jain K, Pathak S, Kumar P, Singh A, Pant RP. Dynamic magneto-optical inversion in magnetic fluid using NanoMOKE. *J Magn Magn Mater*. 2019;475:782-786. doi:10.1016/j.jmmm.2018.12.039

[4] Kumar P, Pathak S, Singh A, et al. Augmented magnetic nanoparticle assimilation in rGO sheets for tailored static and dynamic magnetic properties in surface functionalized Co0.8Zn0.2Fe2O4 nanoferrite-rGO hybrid structures. *J Mater Chem C*. Published online 2024:18036-18047. doi:10.1039/d4tc03498h

[5] Singh A, Kumar P, Pathak S, et al. Tailored nanoparticles for magnetic hyperthermia: Highly stable aqueous dispersion of Mn-substituted magnetite superparamagnetic nanoparticles by double surfactant coating for improved heating efficiency. *J Alloys Compd*. 2024;976:172999. doi:https://doi.org/10.1016/j.jallcom.2023.172999

[6] Kumar P, Pathak S, Singh A, et al. Optimization of cobalt concentration for improved magnetic characteristics and stability of CoxFe3-xO4 mixed ferrite nanomagnetic fluids. *Mater Chem Phys*. 2021;265:124476. doi:10.1016/j.matchemphys.2021.124476

[7] Kumar P, Pathak S, Singh A, et al. Enhanced static and dynamic magnetic properties of PEG-400 coated CoFe2−xErxO4 (0.7≤ x≤ 0) nanoferrites. *J Alloys Compd*. 2021;887:161418.

[8] Jahan N, Pathak S, Jain K, Pant RP. Enchancment in viscoelastic properties of flake-shaped iron based magnetorheological fluid using ferrofluid. *Colloids Surfaces A Physicochem Eng Asp*. 2017;529:88-94.

[9] Mishra A, Pathak S, Kumar P, et al. Measurement of Static and Dynamic Magneto-Viscoelasticity in Facile Varying pH Synthesized CoFe 2 O 4 -Based Magnetic Fluid. *IEEE Trans Magn*. 2019;55(12):1-7. doi:10.1109/TMAG.2019.2936802

[10] Kumar P, Pathak S, Singh A, et al. Effect of post annealing process on structural, magnetic and spin dynamics properties of MnFe2O4 nanoparticles. *Mater Today Proc*. Published online 2023. doi:https://doi.org/10.1016/j.matpr.2023.05.456

[11] Pathak S, Jain K, Kumar P, Wang X, Pant RP. Improved thermal performance of annular fi n-shell tube storage system using magnetic fl uid. *Appl Energy*. 2019;239(May 2018):1524-1535. doi:10.1016/j.apenergy.2019.01.098

[12] Singh A, Pathak S, Kumar P, et al. Tuning the magnetocrystalline anisotropy and spin dynamics in CoxZn1-xFe2O4 ($0 \leq x \leq 1$) nanoferrites. *J Magn Magn Mater*. 2020;493:165737. doi:10.1016/j.jmmm.2019.165737

[13] Pathak S, Verma R, Kumar P, et al. Facile Synthesis, Static, and Dynamic Magnetic Characteristics of Varying Size Double-Surfactant-Coated Mesoscopic Magnetic Nanoparticles Dispersed Stable Aqueous Magnetic Fluids. *Nanomaterials*. 2021;11(11):3009. doi:10.3390/nano11113009

[14] Pathak S, Verma R, Singhal S, et al. Spin dynamics investigations of multifunctional ambient scalable Fe3O4 surface decorated ZnO magnetic nanocomposite using FMR. *Sci Rep*. 2021;11(1). doi:10.1038/s41598-021-83394-8

[15] Pathak S, Jain K, Kumar P, Wang X, Pant RP. Improved thermal performance of annular fin-shell tube storage system using magnetic fluid. *Appl Energy*. 2019;239:1524-1535. doi:10.1016/J.APENERGY.2019.01.098

[16] Kharat PB, Somvanshi SB, Somwanshi SB, Mopari AM. Synthesis, characterization and hyperthermic evaluation of PEGylated superparamagnetic MnFe2O4 ferrite nanoparticles for cancer therapeutics applications. In: *Macromolecular Symposia*. Vol 400. Wiley Online Library; 2021:2100130.

[17] Pathak S, Jain K, Kumar V, Pant RP. Magnetic fluid based high precision temperature sensor. *IEEE Sens J*. 2017;17(9):2670-2675.

[18] Pant RP, Singh VN, Jain K, Gautam A. *Material Aspects of Ferrofluids*.; 2023. doi:10.1201/9781003274247

[19] Albino M, Fantechi E, Innocenti C, et al. Role of Zn2+ Substitution on the Magnetic, Hyperthermic, and Relaxometric Properties of Cobalt Ferrite Nanoparticles. *J Phys Chem C*. 2019;123(10):6148-6157. doi:10.1021/acs.jpcc.8b10998

[20] Yaseneva P, Bowker M, Hutchings G. Structural and magnetic properties of Zn-substituted cobalt ferrites prepared by co-precipitation method. *Phys Chem Chem Phys*. 2011;13(41):18609-18614.

[21] Fantechi E, Innocenti C, Zanardelli M, et al. A smart platform for hyperthermia application in cancer treatment: Cobalt-doped ferrite nanoparticles mineralized in human ferritin cages. *ACS Nano*. 2014;8(5):4705-4719. doi:10.1021/nn500454n

[22] Ma Y, Xia J, Yao C, et al. Precisely Tuning the Contrast Properties of Zn x Fe3–x O4 Nanoparticles in Magnetic Resonance Imaging by Controlling Their Doping Content and Size. *Chem Mater*. 2019;31(18):7255-7264.

[23] Victory M, Pant RP, Phanjoubam S. Synthesis and characterization of oleic acid coated Fe–Mn ferrite based ferrofluid. *Mater Chem Phys*. 2020;240:122210.

[24] Gawas SG, Meena SS, Yusuf SM, Verenkar VMS. Anisotropy and domain state dependent enhancement of single domain ferrimagnetism in cobalt substituted Ni–Zn ferrites. *New J Chem*. 2016;40(11):9275-9284.

[25] Zufelato N, Aquino VRR, Shrivastava N, Mendanha S, Miotto R, Bakuzis AF. Heat Generation in Magnetic Hyperthermia by Manganese Ferrite-Based Nanoparticles Arises from Neel Collective Magnetic Relaxation. *ACS Appl Nano Mater*. 2022;5(5):7521-7539.

[26] Salih SJ, Mahmood WM. Review on magnetic spinel ferrite (MFe2O4) nanoparticles: From synthesis to application. *Heliyon*. Published online 2023.

[27] Pham TN, Huy TQ, Le AT. Spinel ferrite (AFe 2 O 4)-based heterostructured designs for lithium-ion battery, environmental monitoring, and biomedical applications. *RSC Adv*. 2020;10(52):31622-31661.

[28] Scherer C, Figueiredo Neto AM. Ferrofluids: properties and applications. *Brazilian J Phys*. 2005;35:718-727.

[29] Modaresi N, Afzalzadeh R, Aslibeiki B, et al. Magnetic properties of Zn x Fe 3−x O 4 nanoparticles: A competition between the effects of size and Zn doping level. *J Magn Magn Mater*. 2019;482:206-218. doi:10.1016/j.jmmm.2019.03.060

[30] Hossain AKMA, Biswas TS, Yanagida T, Tanaka H, Tabata H, Kawai T. Investigation of structural and magnetic

properties of polycrystalline Ni0. 50Zn0. 50− xMgxFe2O4 spinel ferrites. *Mater Chem Phys*. 2010;120(2-3):461-467.

[31] Varghese D, S. R N, P JSJ, S M, J M, M VAR. Synergistic design of CuO/$CoFe_2O_4$/MWCNTs ternary nanocomposite for enhanced photocatalytic degradation of tetracycline under visible light. *Sci Rep*. 2025;15(1):320. doi:10.1038/s41598-024-82926-2

[32] Vinod S, Philip J. Thermal and rheological properties of magnetic nanofluids: Recent advances and future directions. *Adv Colloid Interface Sci*. 2022;307(June):102729. doi:10.1016/j.cis.2022.102729

[33] Davies GA, Stokes JR. On the gap error in parallel plate rheometry that arises from the presence of air when zeroing the gap. *J Rheol (N Y N Y)*. 2005;49(4):919-922.

[34] Paul G, Kumar Das P, Manna I. Synthesis, characterization and studies on magneto-viscous properties of magnetite dispersed water based nanofluids. *J Magn Magn Mater*. 2016;404:29-39. doi:10.1016/j.jmmm.2015.11.085

[35] Odenbach S. Recent progress in magnetic fluid research. *J Phys Condens Matter*. 2004;16(32). doi:10.1088/0953-8984/16/32/R02

[36] Roberts GP, Barnes HA, Carew P. Modelling the flow behaviour of very shear-thinning liquids. *Chem Eng Sci*. 2001;56(19):5617-5623. doi:10.1016/S0009-2509(01)00291-3

[37] Singh A. Insight on efficient biocompatible magnetic nanoparticles for cancer treatment using magnetic hyperthermia technique. In: *Material Aspects of Ferrofluids*. CRC Press; 2023:247-249.

[38] Sivaranjani KS, Jacob GA, Joseyphus RJ. Comprehensive Law-of-Approach-to-Saturation for the Determination of Magnetic Anisotropy in Soft Magnetic Materials. *Phys status solidi*. 2022;259(10):2200050.

[39] Vékás L. Ferrofluids and magnetorheological fluids. *Adv Sci Technol*. 2009;54:127-136.

[40] Salahuddin T, Awais M. A comparative study of Cross and Carreau fluid models having variable fluid characteristics. *Int Commun Heat Mass Transf*. 2022;139:106431.

[41] Carreau PJ. Rheological equations from molecular network theories. *Trans Soc Rheol*. 1972;16(1):99-127.